GEOPHYSICS, VOL. 70, NO. 5 (SEPTEMBER-OCTOBER 2005); P. B19–B34, 14 FIGS., 4 TABLES.
10.1190/1.2073887

Case History

Gas hydrates at the Storegga Slide: Constraints from an analysis of multicomponent, wide-angle seismic data

Stefan Bünz[1], Jürgen Mienert[1], Maarten Vanneste[1], and Karin Andreassen[1]

ABSTRACT

Geophysical evidence for gas hydrates is widespread along the northern flank of the Storegga Slide on the mid-Norwegian margin. Bottom-simulating reflectors (BSR) at the base of the gas hydrate stability zone cover an area of approximately 4000 km^2, outside but also inside the Storegga Slide scar area. Traveltime inversion and forward modeling of multicomponent wide-angle seismic data result in detailed P- and S-wave velocities of hydrate- and gas-bearing sediment layers. The relationship between the velocities constrains the background velocity model for a hydrate-free, gas-free case. The seismic velocities indicate that hydrate concentrations in the pore space of sediments range between 3% and 6% in a zone that is as much as 50 m thick overlying the BSR. Hydrates are most likely disseminated, neither cementing the sediment matrix nor affecting the stiffness of the matrix noticeably. Average free-gas concentrations beneath the hydrate stability zone are approximately 0.4% to 0.8% of the pore volume, assuming a homogeneous gas distribution. The free-gas zone underneath the BSR is about 80 m thick. Amplitude and reflectivity analyses suggest a rather complex distribution of gas along specific sedimentary strata rather than along the base of the gas hydrate stability zone (BGHS). This gives rise to enhanced reflections that terminate at the BGHS. The stratigraphic control on gas distribution forces the gas concentration to increase slightly with depth at certain locations. Gas-bearing layers can be as thin as 2 m.

INTRODUCTION

In recent years, gas hydrates on the mid-Norwegian margin have drawn considerable attention because they exist at the sidewall of the 90 000-km^2 submarine Storegga Slide. The slide is situated above deepwater hydrocarbon reservoirs that are to be exploited by the Norwegian hydrocarbon industry. A relationship between gas hydrate dissociation and slope failure has been suggested (Mienert et al., 1998). Analyses of new geophysical data in combination with hydrate stability modeling indicate that the gas hydrate field is highly mobile (Mienert et al., 2001; Berndt et al., 2002) and might have played a key role in the initiation of individual sliding phases during postglacial (Holocene) ocean warming (Vogt and Jung, 2002). Furthermore, landslides may set off large tsunamis (Bondevik et al., 1997; Ward, 2001) that threaten coastal lowlands. Apart from being a geological hazard, the worldwide presence of gas hydrates in continental margin and permafrost areas in combination with their high methane concentration make them a potential future energy resource. They might also be a likely source of methane, which contributes to global warming (Kvenvolden, 1993; Kennett et al., 2003).

Gas hydrates are icelike crystals that form a hydrogen-bonded cage of water molecules and entrap small-molecular-weight hydrocarbon and nonhydrocarbon gas molecules (Sloan, 1998). Natural gas hydrate accumulations have commonly been inferred on seismic reflection profiles from the presence of a bottom-simulating reflector (BSR, see Table 1) at the base of the mostly pressure-temperature-controlled gas hydrate stability zone (GHSZ). The GHSZ usually comprises the upper few hundred meters of continental margin sediments. The BSR originates from the strong impedance contrast between sediments containing gas hydrates above and

Manuscript received by the Editor April 27, 2004; revised manuscript received December 31, 2004; published online September 14, 2005.
[1]University of Tromsø, Department of Geology, Dramsveien 201, 9037 Tromsø, Norway. E-mail: stefan.buenz@ig.uit.no; juergen.mienert@ig.uit.no; maarten.vanneste@ig.uit.no; karin.andreassen@ig.uit.no.

gas that is trapped in the sediments below the hydrate. The BSR is primarily generated by the low velocities caused by the presence of gas beneath gas hydrates; thus, the absence of a BSR does not necessarily imply the absence of gas hydrates (Holbrook et al., 1996; Holbrook, 2000).

A continuous BSR exists along most of the northern flank of the Storegga Slide as well as within the slide area (Bünz et al., 2003). The spatial correlation of BSR-inferred gas hydrate occurrence and landslide area alone is insufficient for a successful analysis of the relationship between gas-hydrate stability and submarine landslides. Information on the distribution of gas hydrates and free gas and an estimate of their concentrations in the sediments would allow a more quantitative assessment of gas hydrate influence on slope failure in the Storegga Slide area. It would also be important to know the approximate amount of methane that could have been released from the hydrate reservoir into the ocean as a consequence of gas hydrate dissociation and whether this could have influenced global climate. Additionally, such detailed analysis can provide further insight into hydrate formation mechanisms on the mid-Norwegian margin.

Analyses of the seismic velocities and amplitude behavior at the BSR provide an efficient way of identifying and characterizing the distribution of gas hydrates within sediments (Hyndman and Spence, 1992; Singh et al., 1993; Katzman et al., 1994; Korenaga et al., 1997). The compressional (P-wave) velocity of pure gas hydrates is very high (3.3–3.8 km/s) (Sloan, 1998). As a result, partially hydrate-bearing sediments have a higher interval velocity than the host sediments alone, while gas-charged sediments have a lower velocity.

Recent technological developments in ocean-bottom seismic (OBS) technology and proper processing methods make it possible to acquire shear-wave (S-wave) data in marine environments (Gaiser et al., 2001; Flüh et al., 2002; Stewart et al., 2002, 2003). The number of applications is large; the most successful one is imaging through gas-obscured areas (MacLeod et al., 1999). The combined analysis of P- and S-waves can be used successfully to characterize lithology and pore fluids and to resolve ambiguities that would result from the analysis of P-wave data alone (Tatham, 1982; Engelmark, 2001). The S-wave velocity is crucial for hydrocarbon detection. In conjunction with P-wave velocity, S-wave velocity may help to discriminate pore fluids. In the case of gas hydrates, the S-wave velocity can be used to distinguish whether hydrates act as cement between the sediment grains or are disseminated in the pore space: S-wave velocities increase in the case of cementation, whereas they do not in the case of disseminated hydrates away from the grain contacts.

The objectives of this paper are (1) to investigate the distribution of gas hydrates and free gas in order to estimate their concentration within the sediments in the immediate vicinity of the Storegga Slide complex on the mid-Norwegian margin and (2) to reveal the nature of the BSR and the enhanced reflections. We use multicomponent, wide-angle OBS and single-channel seismic (SCS) data to constrain seismic velocities of the sediments by traveltime inversion and ray-trace forward modeling. Seismic velocities allow us to estimate the concentration of hydrates and gas. The velocity results are integrated with amplitude analyses to assess the nature of the BSR and the enhanced reflections. An ocean-bottom cable (OBC) data set (Andreassen et al., 2003; Bünz and Mienert, 2004) facilitates a reliable correlation of events on P-wave and converted-wave (C-wave) components.

Table 1. Glossary of abbreviations.

Abbreviation	Definition
OBC	Ocean-bottom cable
OBS	Ocean-bottom seismometer/seismic
BSR	Bottom-simulating reflector
GHSZ	Gas hydrate stability zone
BGHS	Base of gas hydrate stability
TWT	Two-way traveltime
SCS	Single-channel seismic
ODP	Texas A&M University's Ocean Drilling Program

GEOLOGIC SETTING

The Møre and the Vøring basins are the two prominent basins on the mid-Norwegian margin (Figure 1). They developed as a result of several rifting episodes until late Paleocene/early Eocene continental break-up and subsequent thermal subsidence (Skogseid and Eldholm, 1989; Brekke, 2000). An episode of moderate compression between late Eocene and middle Miocene times led to the development of north-south-oriented dome structures (see Figure 2 in Bünz et al., 2003),

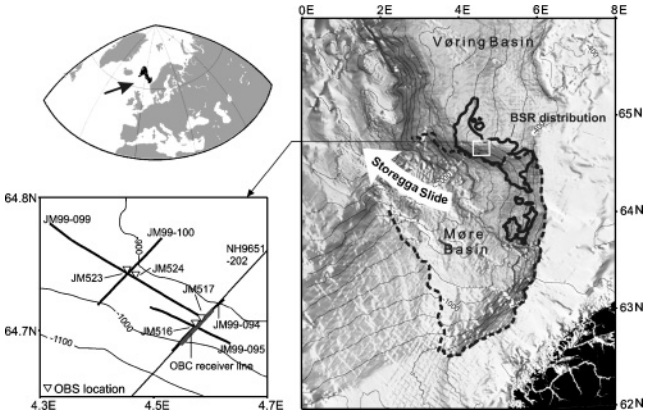

Figure 1. Distribution of the BSR on the mid-Norwegian margin and location of OBS, OBC, and single-channel seismic data. The dashed line delineates the extent of the Storegga Slide within the Møre Basin. After Bünz et al. (2003).

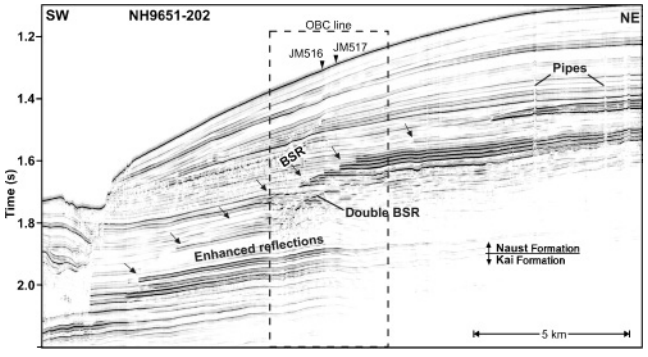

Figure 2. Examples of the BSR on the mid-Norwegian margin. The BSR is mainly identified as the termination of enhanced reflections. Only at the location of the OBC line does it show as a continuous reflection. The dashed line marks the location of the OBC line; the triangles mark OBS positions.

which are known to be potential hydrocarbon reservoirs, e.g., the Ormen Lange gas reservoir (Brekke and Riis, 1987; Doré and Lundin, 1996; Bryn et al., 1998; Vågnes et al., 1998). The second-youngest sedimentary succession comprises the Miocene/earliest Pliocene Kai Formation, with predominantly fine-grained hemipelagic sediments (Dalland et al., 1988; Blystad et al., 1995; Rokoengen et al., 1995). The overlying Naust Formation encompasses sediments of the Pliocene-Pleistocene glacial-interglacial cycles that significantly changed the sedimentation pattern, yielding a thick wedge of clastic sediments on the shelf (Stuevold and Eldholm, 1996; Hjelstuen et al., 1999). Current-controlled drift sediments (contourites) deposited along slope during deglaciation and interglacials frequently interlayer the glaciogenic downslope-transported debris flows (Rokoengen et al., 1995; Laberg et al., 2001; Evans et al., 2002).

The Storegga Slide complex is situated in large parts of the Møre basin and the southern Vøring basin (Bugge et al., 1988; Bryn et al., 2003). This multiphase submarine landslide happened 8200 years ago (Haflidason et al., 2004) and remobilized the sediments of the Naust Formation, partly removing up to 450 m of sedimentary strata. The eastern headwall runs north to south and reaches a height of up to 300 m. The northern sidewall is up to 100 m high and runs roughly east to west along the border between the Vøring and the Møre basins. The triggering mechanism is possibly a combination of various effects, e.g., gas hydrate dissociation and earthquakes. Bugge et al. (1988) and Mienert et al. (1998) suggest that gas hydrate dissociation contributes to slope instability. Bryn et al. (2003) reports that the overall development of the slide is retrogressive and that repeated large-scale sliding during the last 500 000 years shows a link to Pleistocene climatic fluctuations.

Mienert et al. (1998) and Posewang and Mienert (1999) identify a gas hydrate–related BSR close to the northern sidewall outside the slide area, while Bouriak et al. (2000) show evidence for such a BSR within the slide area. Bünz et al. (2003) map this characteristic reflection within the sediments of the southern Vøring and the Møre basins in detail. The BSR runs parallel to the sea floor and crosscuts the sediment strata. The BSR is generally characterized by an abrupt termination of enhanced reflection amplitudes underneath (Figure 2). The most continuous BSR occurs along the northern flank of the Storegga Slide and extends into the northeastern corner of the slide (Figure 1). The distribution of the BSR on the mid-Norwegian margin is strongly controlled by the properties of gas hydrate host sediments (Bünz et al., 2003). Glaciogenic debris-flow deposits to the north inhibit gas hydrate growth and/or gas migration into the GHSZ; hence, the formation of a BSR (Bünz et al., 2003). In the west, the lithologic composition of preglacial basin deposits of the Kai Formation does not allow the growth of gas hydrates because of the fine-grained sediment composition (Bünz et al., 2003). Furthermore, the formation of a polygonal fault system (Berndt et al., 2003) has considerably reduced pore size and water content of the sediments, making them unsuitable to host gas hydrates. The BSR only occurs within the contouritic and hemipelagic deposits of the Naust Formation, which seem to be conducive to gas hydrate growth. The gas hydrate stability conditions exclude gas hydrates on the continental shelf because bottom-water temperatures are too high (Mienert et al., 2001). Bouriak et al. (2000) and Bünz et al. (2003) suggest that the Storegga gas hydrates develop from fluids that originate far beneath the GHSZ.

Bünz and Mienert (2004) preliminarily estimate gas hydrate saturation in this area based on P-wave velocity analysis of OBC data to an average of 4% to 5% of pore volume. The gas hydrates at Storegga were drilled in 1997 (Mienert and Bryn, 1997; Norwegian Geotechnical Institute, 1997). The geotechnical borehole located at OBS JM516 (Figure 1) penetrated the BSR to a depth of 310 m and should have retrieved gas hydrates in small concentrations just above the BSR. The fact that gas hydrates could not be recovered (Mienert and Bryn, 1997) suggests that hydrates must have been dissociated as a result of the coring activity. Ocean Drilling Program Leg 204 undoubtedly demonstrated the need for pressure coring to recover gas hydrates from subbottom sediments (Tréhu et al., 2002). The borehole mainly provides geotechnical parameters for slope stability assessments (Norwegian Geotechnical Institute, 1997) that are also useful for rock physics modeling.

SEISMIC DATA

The seismic data used in this study were acquired from the R/V *Jan Mayen* in 1999. The acoustic source was an air gun array consisting of two 40 in^3 sleeve guns with a main frequency around 100 Hz. A number of single-channel seismic (SCS) profiles were shot in the upslope direction and were used for delineating the BSR distribution (Bünz et al., 2003). These profiles also provided onboard information for exact positioning of the multicomponent OBS systems. Four OBS stations were selected in water depths between 850 and 1000 m (Figure 1). Two were deployed along an OBC line acquired previously (Figures 1–3) (Andreassen et al., 2003). Three seismic lines were shot across the OBS stations. Line JM99-094 (Figure 4a) runs along the OBC line in the upslope direction and crosses OBS JM516 and OBS JM517. Lines JM99-095 (Figure 4b) and JM99-099 (Figure 4c) run along the slope and cross OBS JM517, OBS JM523, and OBS JM524, respectively.

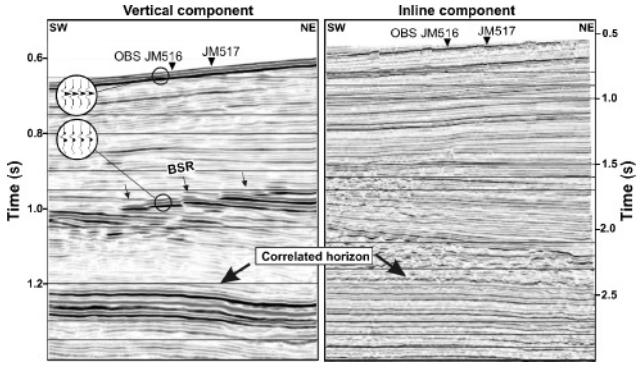

Figure 3. The P-wave stack (vertical component) and PS-wave stack (inline component) of the OBC line, which is approximately 4 km long. Note the difference in the time axes. The inline component has been stretched linearly in time based on the indicated horizon, which occurs just below a sedimentary bed with chaotic internal texture. The triangles mark the location of the OBS. The center part of the vertical component shows the BSR as a reflection proper, which is phase reversed when compared with the seafloor reflection.

The processing of all of the SCS lines included a spherical divergence correction, spiking deconvolution, Ormsby bandpass filtering (30–300 Hz), and Stolt migration.

The OBS data were relocated using shot-time information of the direct wave. Subsequently, the three-component (3C) data sets were rotated to take into account the orientation of the seismometer on the seafloor (Gaiser, 1999). The first-break arrival was analyzed for the receiver orientation. The highest signal quality could be achieved when all three components were included in the rotation. The seismic processing of the hydrophone, the vertical component, and the inline component include amplitude corrections for spherical divergence and inelastic attenuation, spiking deconvolution, and Ormsby bandpass filtering (30–250 Hz).

The OBC data (Figure 3) were acquired by Petroleum GeoServices (PGS) using a single air gun with a volume of 3080 in^3, i.e., 40 times larger than that used for the OBS data. We refer the reader to Andreassen et al. (2003), who discuss in detail the processing results of the OBC line, which included a prestack bandpass filter (3–125 Hz), true amplitude recovery, predictive deconvolution, NMO correction, time-variant scaling, stacking, poststack scaling, and, again, filtering. In this paper, we use the vertical and inline component of the OBC data. The vertical component records vertical displacements of the seafloor and principally provides an image of the subseafloor derived from the P-waves. The inline component records horizontal displacements in the direction of the survey and principally provides an image of the subseafloor that results from converted waves (C- or PS-waves), i.e., waves that propagate downward as P-waves and then convert to upward-propagating S-waves at a lithologic boundary whenever the angle of incidence is not zero. Theoretically, the number of conversions for each generated wave type is indefinite, but the loss of energy during reflection, transmission, or conversion is high, and the recording of wave types other than pure PS is unlikely (Engelmark, 2001).

To facilitate the amplitude analysis, relative-amplitude-preserving processing must be applied to the OBS and SCS data. Because of the OBS acquisition geometry, shot-to-shot variations of source strength must be removed before AVO analysis can be performed (Müller et al., 2001). This correction is applied after the data have been corrected for spherical divergence and inelastic attenuation by a time to the power of one (t^1) scaling function. The source array, consisting of two parallel-towed sleeve guns, can be considered a point source, and the OBS resembles a point receiver on the seafloor. No directivity corrections need to be applied. The SCS data were corrected by a t^1 scaling function to compensate for loss of amplitude from wavefront spreading and inelastic attenuation.

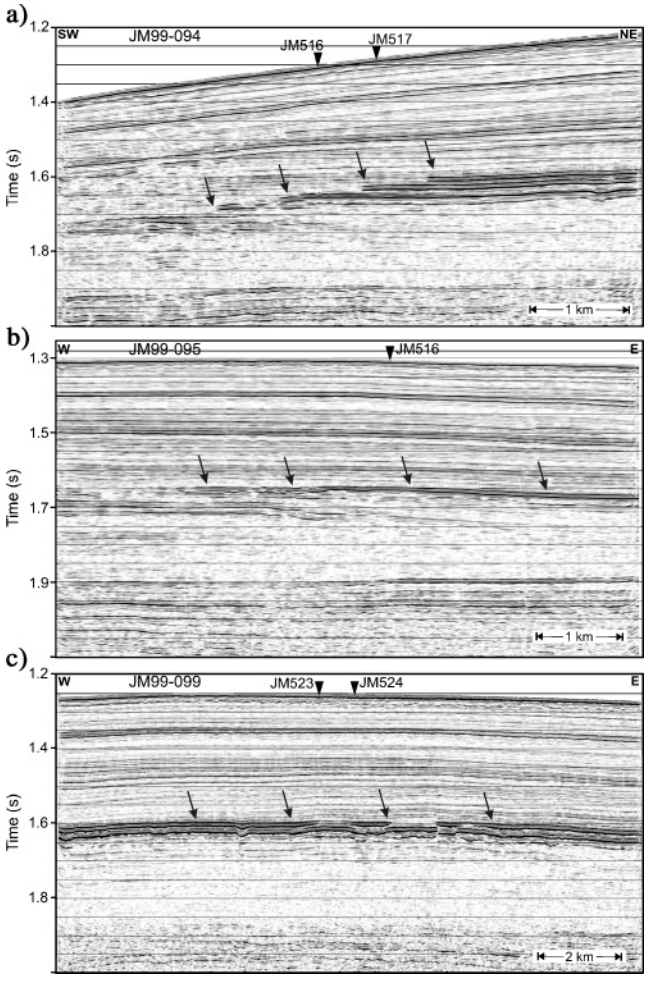

Figure 4. SCS lines (a) JJ99-094, (b) JJ99-095, and (c) JJ99-099, with locations of the OBS, noted by inverted triangles. Arrows mark the BSR.

SEISMIC OBSERVATIONS

Profile JM99-094 (Figure 4a) shows the typical expression of the BSR in the study area. The BSR marks the upward termination of enhanced reflections, and its position lies at the theoretically predicted depth (Mienert et al., 2001), mimicking the seafloor topography. The upward termination of these enhanced reflections was used to map the BSR distribution laterally (Bünz et al., 2003). The amplitude of the enhanced reflection varies considerably along the line. In contrast, the vertical component of the OBC line at the same location (Figure 3) exhibits parts of the BSR as a reflection proper rather than reflection-amplitude variations. This difference in appearance is explained by the lower main frequency content (30–50 Hz), which results in the lower resolution of the OBC data. Also, the BSR on the OBC line shows a clear phase reversal compared to the seafloor reflection. The BSR on lines JM99-095 and JM99-099 is marked by high-amplitude reflections at about 1.65 and 1.60 s two-way traveltime (TWT), respectively. Here, the BSR runs almost parallel to the bedding, but it also shows significant changes in amplitude and waveform.

The inline component of the OBC line (Figure 3) allows for a visual correlation, with the image of the vertical component based on a marked acoustic horizon. This component provides much better resolution of the stratigraphy than the vertical component, a consequence of the lower velocity of S-waves compared to P-waves. A BSR is not observed on the inline component of the OBC line. However, underneath the approximate position of the BSR, the inline component gives a much better image of the subsurface than the vertical component.

On the OBC data, seismic reflections can be identified to a greater depth than on the OBS records (Figure 5). This is a result of the much larger source of the OBC setup. Apparently, the larger air gun source also causes larger wave conversions because the inline component of the OBC data shows more arrivals than its OBS counterpart (Figure 5). The main frequency band of the inline component of the OBS data is shifted to lower frequencies (15–30 Hz) compared to the vertical component (80–100 Hz). This might result from stronger attenuation of higher frequencies in the S-mode, especially within the uppermost unconsolidated sediments of the seafloor, where S-wave velocities are very low and a high S-wave velocity gradient exists (Hamilton, 1976).

VELOCITY ANALYSIS

To infer the occurrence of gas hydrate and free gas within the sediments, we analyze the vertical velocity variation based on traveltime picks. The inversion of traveltimes provides average velocities for individual layers and enables us to estimate average concentrations of gas hydrate and free gas at the northern flank of the Storegga Slide.

We used traveltime inversion (Zelt and Smith, 1992) to determine the P-wave velocity model at all OBS stations. Multicomponent OBS stations JM516 and JM517 coincide with the location of an OBC line (Figure 3), providing an excellent opportunity to compare and correlate the C-wave component of the individual OBS components with the OBC data. Subsequently, we can determine an S-wave velocity model for the uppermost 600 m of the sediments by applying ray-trace forward modeling. The P- and S-wave velocities can be used to determine a background velocity model, which somewhat substitutes hydrates and gas within the pore spaces with brine. This background velocity model for hydrate- and gas-free sediments can in turn be used to estimate gas hydrate and gas saturations. Although S-wave velocities can be assessed indirectly by AVO analysis of the P-wave component, the direct evaluation of the pure shear mode (SS) or converted mode (PS) provides more accurate information. This assertion especially holds for unconsolidated rocks of the shallow subsurface (<1000 m), where the AVO behavior is dominated by the pore fluid. Figure 6 schematically summarizes the steps of the analyses of P- and S-wave velocity.

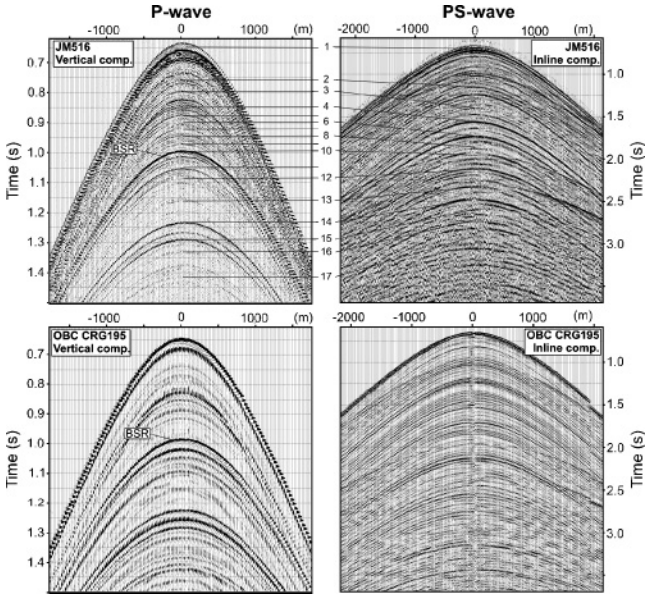

Figure 5. Vertical and inline component of the OBS JM516 data set and OBC CRG195. Horizons used during the traveltime inversion and modeling of the OBS data are indicated and numbered as referred to in the text.

Methodology

Traveltime inversion of P-wave component

For each OBS station, we determined a preliminary velocity-depth model using standard semblance analysis. However, considering that common receiver gathers (CRGs) are not common depth gathers (CDPs), one should take into account the subsurface geometry. Semblance analysis assumes horizontal layering of the geologic strata. This assumption leads to errors in the determined velocity-depth functions in areas with dipping reflectors.

The high-resolution SCS and OBS data show several reflections above the BSR (Figures 4 and 5). Only a few reflections are visible underneath the BSR, in a zone with a more transparent character (Figure 4) where gas-laden fluids are supposed to rise (Bouriak et al., 2000; Bünz et al., 2003). A correlation of events from SCS to OBS data can be well established. Corresponding horizons were picked on

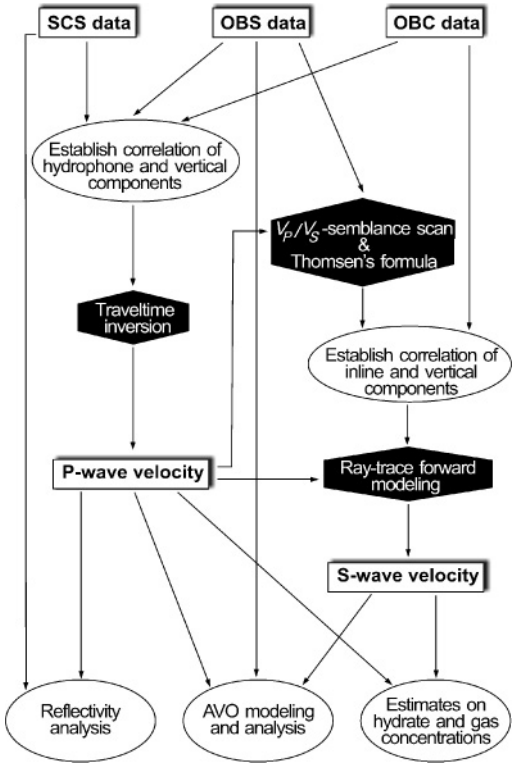

Figure 6. Flowchart summarizing the different steps used to constrain P- and S-wave velocities that result in the estimates of hydrate and gas concentrations.

the SCS and OBS data. The starting velocity-depth model for the traveltime inversion was determined by converting the picked horizons of the SCS sections from time to depth using the preliminary velocity-depth model based on the semblance analysis. A least-squares damped inversion of traveltimes (Zelt and Smith, 1992) yielded the 1D velocity-depth structure at the OBS positions. The inversion also accounted for the subseafloor geometry of slightly dipping reflections. The maximum dip of 1.2° occurs for the shallow reflections on line JM99-094 (Figure 4a). The subsurface geometry on lines JM99-095 and JM99-099 is almost horizontally layered (Figure 4b, c).

We followed a procedure in which layers were inverted in a layer-stripping approach from the top to the bottom (Zelt and Forsyth, 1994). In the first phase, we inverted only the seafloor, the BSR, two horizons in between, and the high-amplitude reflection at the base of the Naust Formation; we introduced the remaining horizons during a second phase of the inversion. No lateral velocity variations or vertical velocity gradients within individual layers were allowed during the inversion. In general, velocities derived from the semblance analysis were already well constrained. The fine-tuned traveltime inversion velocity–depth models for all OBS differ by less than 5 m in depth and 30 m/s in velocity. This corroborates the use of semblance analysis followed by traveltime inversion in favor of a forward-modeling technique. Calculated traveltimes generally match the observed traveltimes (for example, the vertical component of OBS JM516 is shown in Figure 7).

We estimated the uncertainties of the inversion according to Katzman et al. (1994), where certain model parameters were perturbed such that the rms traveltime residual increased until it exceeded the pick uncertainty (4 ms). This resulted in an average velocity error of ±50 m/s and an average depth error of 5 m. However, the traveltime residual of the best-fit model was 1 ms (individual horizons are 1 to 3 ms), which is significantly lower than the estimated pick uncertainty (4 ms). Therefore, we assume that actual errors are much below the above-mentioned velocity and depth errors, which represent the absolute maximum error bounds. Concentrating on the layer directly overlying the distinct BSR (reflection 10, Figure 5), we estimated the error on the inferred velocity at 25 m/s. Finally, to reduce the uncertainty, we averaged the velocity models from hydrophone and vertical components of each station and line.

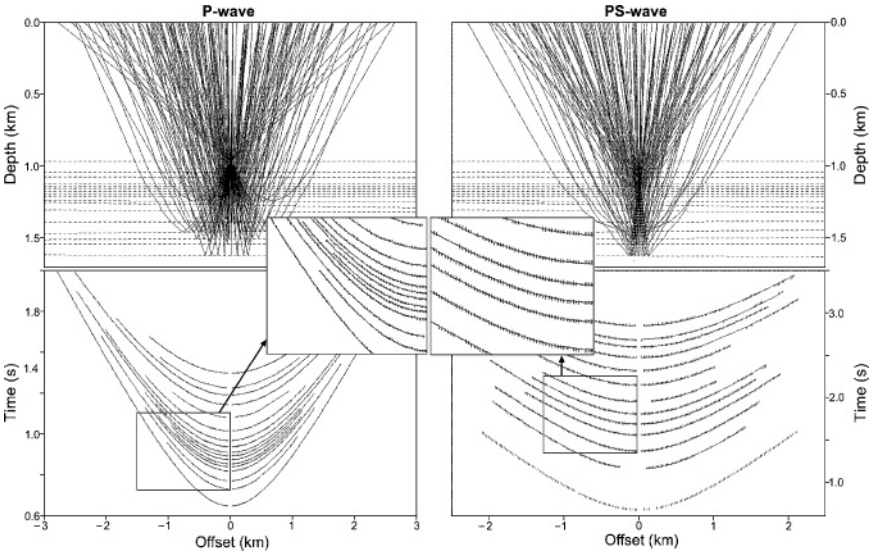

Figure 7. Traveltime inversion and modeling of P- and PS-wave components of the OBS JM516 data set.

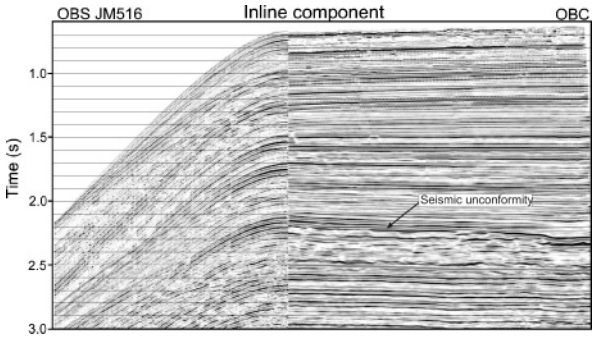

Figure 8. Comparison of the inline component of the OBS JM516 data set and the inline stack of the OBC line. Only the part of the OBC line extending northeastward from the OBS location (Figure 3) is shown. Several horizons show good agreement. The seismic unconformity is an especially strong reflection on both data sets, whereas it is hardly detectable on the P-wave component of the SCS, OBC, and OBS data (Figures 2–5).

Analysis of C-wave component

Estimating the S-wave velocity relies heavily on the correlation of events on P- and C-wave components and is complicated by the fact that such images have different timescales (Figure 3). The correlation is not always straightforward because some interfaces generate PP and PS reflections with the same polarity while others generate reflections with opposite polarity. Also, reflection strength may vary between P- and C-wave recordings.

During the correlation procedure, we assumed that corresponding reflections on both components originated from the same lithologic horizon. We conducted the evaluation of the S-wave velocities for OBS JM516 along line JM99-095 (Figure 4b), which has an almost horizontally layered subsurface. Because OBS JM516 was deployed on the OBC line (Figure 3) located approximately perpendicular to line JM99-095 (Figure 1), events were correlated using the vertical and inline components of the OBS and OBC lines and SCS lines JM99-094 and JM99-095. We were guided by the OBC line interpretation of Andreassen et al. (2003) but added several horizons because the SCS and OBS data showed higher resolution than the OBC data. Horizons on the inline component of the OBS and OBC data generally matched well (Figure 8). The reflection from the top of a chaotic unit, denoted Seismic unconformity (Figure 8), was especially strong on both data sets. The 2D images of the OBC data significantly alleviated

the correlation process of P- and C-wave components because their lateral continuity allowed us to unambiguously identify characteristic features of corresponding horizons.

Furthermore, to facilitate a direct and independent correlation, we carried out a semblance V_P/V_S scan (Figure 9) on the C-wave component and used the derived V_P/V_S ratios to convert the C-wave section from C-wave time to P-wave time. This substantially improved the correlation process (Figures 5 and 9). The V_P/V_S scan worked in very similar fashion to the semblance velocity analysis. The OBS data were corrected by a nonhyperbolic moveout (Thomsen, 1999) using constant V_P/V_S ratios and using the P-wave velocity-depth structure determined by the traveltime inversion. The NMO-corrected OBS data were subsequently stacked and plotted for different V_P/V_S ratios (Figure 9). Correct V_P/V_S ratios showed highest energies because they flatten C-wave arrivals best. Additionally, applying nonhyperbolic moveout corrections to the C-wave data during the semblance analysis further helped discriminate between pure PS mode and other wave types, e.g., conversion upon transmission at the seafloor, multiple conversions, or peg-leg multiples.

The V_P/V_S ratios from the semblance scan correspond to V_P/V_S ratios of short-spread moveout velocities γ_2 (Thomsen, 1999). The correlation of reflections on P- and C-wave sections allows us to calculate a V_P/V_S ratio of average vertical velocities γ_0 from zero-offset traveltimes. Although the zero-offset amplitude for S-waves was expected to be zero (Aki and Richards, 2002), our data showed small energies on near-zero-offset traces, arising from the fact that we did not exactly cross the OBS. Offsets, however, were small enough (38 m) that observed traveltimes were approximately equivalent to zero-offset times. Thus, we were able to pick zero-offset times. Using Thomsen's formula (1999), we subsequently estimated the effective V_P/V_S ratio (γ_{eff}) by

$$\gamma_{eff} = \frac{\gamma_2^2}{\gamma_0}. \quad (1)$$

Knowing γ_{eff} also improves the process of identifying corresponding reflections. If γ_{eff} values are too high or too low, then the corresponding correlation is unlikely. This requires knowing what values are reasonable for γ_{eff}. Generally, the trend of the V_P/V_S scan (γ_2) is a good indicator of how the V_P/V_S ratio changes with depth. As an example, using Thomsen's formula for a reflection at approximately the depth of the BSR, we find a γ_2 of 5.3 and a γ_0 of 6.8, resulting in $\gamma_{eff} = 4.1$. For the reflection interpreted from the base of the gas-bearing sediments underneath the BSR, we found $\gamma_2 = 4.4$ and $\gamma_0 = 6.4$, resulting in $\gamma_{eff} = 3.0$. This quick estimate of V_P/V_S showed a strong drop in V_P/V_S across the BSR interface, which might be attributed to the presence of free gas (Tatham and Stoffa, 1976) trapped within the sediments underneath the hydrates.

Once a final correlation was established, we picked reflections on the C-wave component that corresponded to reflections on the P-wave component (Figures 5 and 9). However, we could not identify correlations for some of the seismic events picked on the P-wave component. For some horizons, the correlation appeared to be uncertain or unreasonable, maybe because the converted waves were not generated — for example, because of a low shear-wave impedance contrast. We decided to use only well-established correlations for the modeling. It is noteworthy that neither the inline component of the OBC (Figure 3) nor the inline component of the OBS data (Figures 5 and 9) showed a BSR. Therefore, we could not pick a C-wave reflection from the BGHS. Instead, we picked a C-wave reflection from a lithologic horizon at corresponding depth. We assumed only a very small uncertainty for this correlation. It allowed us to resolve V_P/V_S ratios for the supposedly hydrate- and gas-bearing zone in greater detail.

We modeled S-wave velocities using the ray-tracing module of Rayinvr software (Zelt and Smith, 1992), keeping the fine-tuned P-wave velocity-depth model fixed such that we perturbed only one parameter, the Poisson's ratio. Rayinvr calculated traveltime residuals. Although those residuals had no meaning quantitatively, they aided qualitatively in finding the best fit between calculated and observed traveltimes. A best fit was determined where traveltime residuals were smallest.

The modeling was conducted in two stages. First, only those horizons (2, 4, 8, 12, and 14; Figure 5) were modeled for which a firm correlation existed. Second, the remaining horizons were introduced, keeping the horizons from the first phase fixed. Generally, a good match was obtained between calculated and observed traveltimes (Figure 7). We estimated the error of the Poisson's ratio in a similar fashion to the P-wave velocity. The Poisson's ratio was perturbed, and calculated traveltimes were evaluated. Once the calculated traveltimes

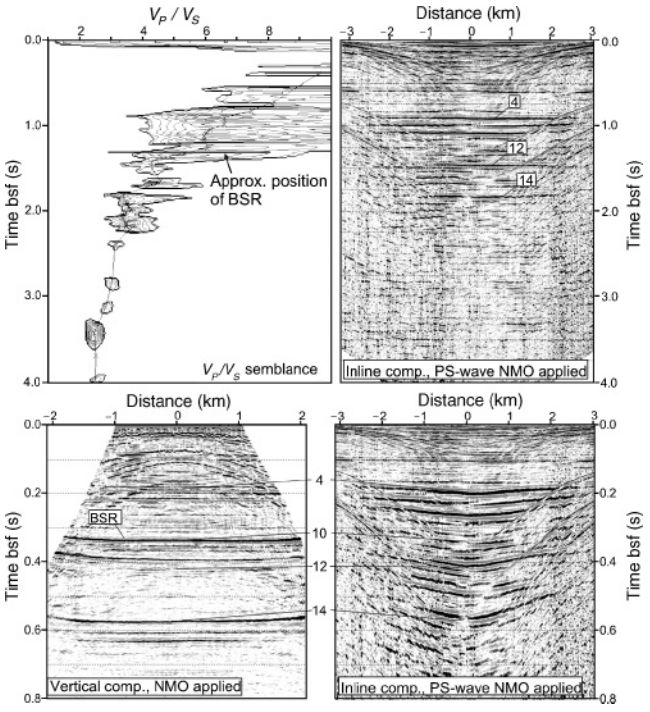

Figure 9. A V_P/V_S semblance scan was applied to the inline component of the OBS JM516 data set to help correlate events on P-wave and C-wave components. The strong decrease of V_P/V_S ratio beneath the BSR position indicates the existence of free gas. Picked V_P/V_S ratios (upper left) optimally flatten horizons on the inline component shown versus C-wave time (upper right) and P-wave time (lower right). The direct-wave traveltime has been subtracted during NMO application and given times are below the seafloor (bsf). Several horizons can be correlated to the vertical component (lower left), and a few key horizons are indicated.

differed from the picked traveltimes by more than the pick uncertainty (10 ms), the error bound was defined. Because the Poisson's ratio is not a linear profile with depth, the error estimate increased with depth from ±0.002 at the seafloor to about ±0.02 at the last modeled horizon. The resulting error estimate for the V_P/V_S ratio, in contrast, decreased with depth from ±1.3 for the uppermost horizon to ±0.3 for the deepest. Consequently, the error for the S-wave velocity varied between 30 and 60 m/s, with an average of approximately 40 m/s, The specific S-wave velocity error for the layer above the BSR was 40 m/s.

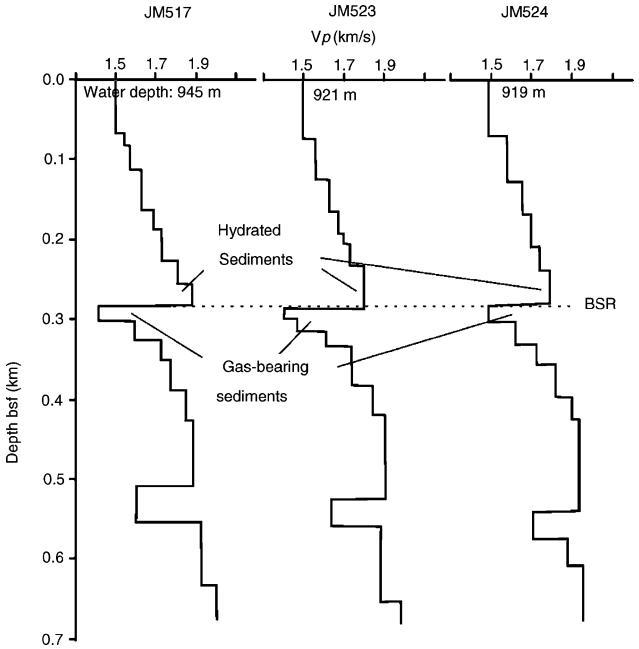

Figure 10. The P-wave velocity-depth profiles for OBS stations JM517, JM523, and JM524. The average error bounds are ±50 m/s in velocity and ±5 m in depth. Depth is measured below the seafloor (bsf).

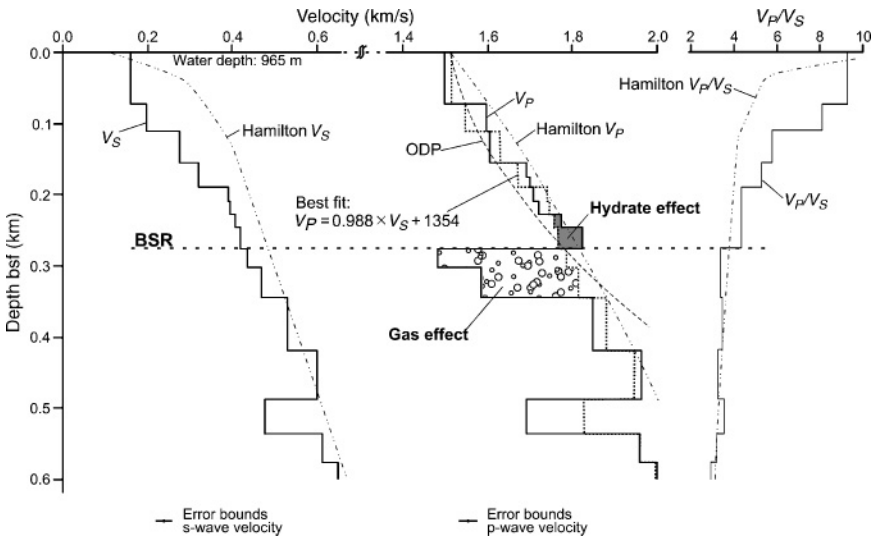

Figure 11. The P- and S-wave velocity profiles and the V_P/V_S ratio profile for OBS JM516 compared to the Hamilton (1979) models and the ODP reference curve for P-wave velocity (Eldholm et al., 1987). The best-fit model marks the P-wave velocity, assuming neither hydrates nor gas is present within the sediments. This model is used to demonstrate the effect of gas hydrates (shaded area) and gas (bubbled area) on the P-wave velocity of the sediments as determined by the traveltime inversion. The average error bounds are ±50 m/s in velocity and ±5 m in depth for P-wave velocity. For S-wave velocity they are ±30–60 m/s in velocity and ±5 m in depth. For the layer above the BSR, the specific error bounds are ±25 m/s and ±40 m/s for P-wave and S-wave velocity, respectively.

Changes of P- and S-wave velocities and V_P/V_S ratios

The traveltime inversion provided average velocities for individual layers with thicknesses between 18 and 97 m. For all stations, P-wave velocities increased gradually with depth down to the predicted BGHS at approximately 280 m below the sea floor (mbsf) (Figures 10 and 11). The P-wave velocities appeared to be higher in an up to 50-m-thick zone just above the BSR. Here, maximum velocities at the four OBS stations varied significantly, between 1791 and 1884 m/s. Beneath the BSR, the P-wave velocity decreased sharply to values of about 1400 to 1500 m/s and thereafter gradually increased to still anomalously low velocities at this depth (1600–1700 m/s). Within this low-velocity zone, minimum velocities at the four OBS stations varied between 1402 and 1490 m/s. The low-velocity-zone thickness had a maximum of about 90 m (OBS station JM517) and was approximately 80 m on average. In the deeper parts, the velocities reached values of 1900 m/s. A second zone of lower P-wave velocities of about 1600 m/s occured at a subbottom depth of 490 mbsf.

The S-wave velocity increased continuously with depth down to about 490 mbsf, where it reached a value of 600 m/s (Figure 11). From 490 to 540 mbsf, a distinct low-S-wave velocity layer exists, which corresponds to the second low-velocity layer observed on the P-wave velocity-depth profile. In contrast to the P-wave profile at the depth of the BGHS, the S-wave velocity profile showed neither positive nor negative velocity deviations. In general, the V_P/V_S ratio showed a strong decrease from about 9 at the seafloor to about 3.4 at 300 mbsf. Below 300 mbsf, it had much less variability and showed small positive and negative deviations.

DISCUSSION

Comparison of velocity changes

We have shown profiles for P-wave and S-wave velocities as well as for V_P/V_S for four locations in an area with a strong BSR on the northern flank of the Storegga Slide. The P-wave profiles show an approximately 40- to 50-m-thick sediment layer with high interval velocities between 1800 and 1900 m/s just above the BSR (Figures 10 and 11). The variation in velocities in this layer is 93 m/s, which significantly exceeds the estimated uncertainty of 25 m/s. All OBS stations are only a maximum of 7 km apart from one another, located in water depths between 919 and 965 m. The lateral velocity variations in

the layer above the BSR are higher than would be expected from lithologic variations over this depth range documented at a geotechnical drill site (Table 2; Norwegian Geophysical Institute, 1997). The seismic data (Figure 4, see also Bünz et al., 2003) and especially the inline component of the OBC line (Figure 3), which is unaffected by fluids, also suggest little if any lithologic variation along the stratigraphic layers (Bünz and Mienert, 2004). Moreover, within the same stratigraphic layer, the velocity above the BSR at OBS JM523 (1815 m/s) differs significantly from the velocity determined at OBS JM516 (1721 m/s). Variation of velocities between OBS stations of shallower layers is well below the velocity uncertainty. This suggests that the lateral velocity variations along the BSR are not caused by lithologic variations within stratigraphic layers. High interval velocities must be explained by another phenomenon. Positive velocity deviations, which occur just above the BGHS, may indicate the existence of an appreciable amount of gas hydrates in the pore space of the sediments. Furthermore, our data suggest the presence of hydrates is confined to the zone just above the BSR, since we do not observe such significant velocity variations within layers elsewhere. This agrees with previous gas hydrate studies on the mid-Norwegian margin (Mienert et al., 1998; Posewang and Mienert, 1999; Andreassen et al., 2000; Bünz and Mienert, 2004).

The P-wave interval velocities in the layer directly underneath the BSR are as low as about 1400 m/s. Below this layer, P-wave velocities are still anomalously low at about 1600 m/s. This distinct decrease in P-wave velocity is attributed to the presence of free gas trapped within the sediments underneath the BGHS. Since the S-wave profile does not have similar deviations at the BSR, the P-wave velocity deviations should be related to the pore fluid and not the sediment matrix. Therefore, the S-wave velocity is unaffected by the composition of the pore fill, regardless of whether it is a mixture of hydrate and brine or gas and brine.

The P-wave velocity results presented here are consistent with earlier studies using forward modeling of OBS data (Mienert et al., 1998; Mienert et al., 2001) and full-waveform inversion of multichannel seismic data (Andreassen et al., 2000). Compressional velocities calculated from the ODP reference curve (Eldholm et al., 1987) form approximately a lower boundary with the exception of the gas-bearing sediments underneath the BSR (Figure 11). Velocities calculated from the Hamilton equation (1979) correspond well to an upper boundary except for the high interval velocity zone overlying the BSR. The ODP Leg 104 sites are 200 km north of the study area, and the Hamilton curve embodies only an average for normally compacted sediments. Both curves fit the data moderately, but they do not represent the velocity trend of the specific geologic setting.

The same holds true for the observed S-wave velocity, which, especially in the shallow part (<300 mbsf), is considerably lower than predicted by the Hamilton equation (1979). The gradual increase of the S-wave velocity down to about 500 mbsf clearly illustrates its depth dependence, as it is primarily controlled by compaction and the number and angularity of the grain contacts (Anstey, 1991). The significant deviation from the Hamilton reference is believed to be related to the specific depositional environment. These sediments were deposited very rapidly by northward-directed contour currents during deglaciation and interglacial/interstadial periods since the middle to late Pleistocene (Laberg et al., 2001; Bryn et al., 2003). Very rapid sedimentation would favor underconsolidation and, therefore, lower S-wave velocities. However, a geotechnical borehole at the site of OBS JM516 shows normally consolidated to slightly overconsolidated sediments (Norwegian Geotechnical Institute, 1997). As a consequence, we need another explanation for the observed low S-wave velocities. This might be found in the high clay content of the sediments (about 50% to 60%) at this site (Norwegian Geotechnical Institute, 1997). In general, the presence of clay softens the rock grain contacts; as the clay content increases, P- and S-wave velocities decrease, but the decrease is higher in S-wave velocity (Han et al., 1986).

Because of the large deviation in V_S, the V_P/V_S curve calculated from our velocity data consequently shows offsets up to five from the Hamilton curve (1979) for the uppermost 280 m of sediment. In the deeper part, the fit is excellent, except that the V_P/V_S ratio of 3.4 for the gas-bearing sediments between 280 and 340 mbsf is probably lower than it would be without gas.

The crossplot of V_S versus V_P (Figure 12) discriminates the hydrate-bearing and gas-bearing sediments from adjacent sediments. The trend differs significantly from the Hamilton trend as well as the mudrock line (Castagna, 1985). The latter is empirically derived from rock samples at the reservoir level and represents only a general model. Therefore, uncertainties exist when applied to the sediments at the northern Storegga Slide flank. No V_P or V_S logs are available that can be used to determine the relationship. Thus, to properly estimate gas hydrate saturations, it is necessary to find other means to determine the background P-wave velocity for hydrate-free sediments. This is achieved by using a specific empirical relationship for our study area derived from our previously determined average P- and S-wave velocities. A least-squares best fit can be calculated from velocities of sediments, ignoring values from the hydrate- or gas-bearing intervals (V_P and V_S given in meters per second), yielding

$$V_P = 0.988 \times V_S + 1354, \quad (2)$$

Table 2. Parameters for rock-physical modeling.

Parameter	Hydrate-bearing sediments	Gas-bearing sediments
Porosity (%)	51	53
Depth below seafloor (m)	270	300
Volumetric fraction of clay (%)	25	20
Volumetric fraction of mica (%)	35	35
Volumetric fraction of calcite (%)	15	15
Volumetric fraction of feldspar (%)	15	20
Volumetric fraction of quartz (%)	10	10
Temperature (°C)	14	15
Salinity (ppm)	32 000	32 000

with a regression coefficient R of 0.987 for the least-squares fit of equation 2.

This relationship is valid only for the regional depositional environment. It also excludes glaciogenic debris-flow deposits because these have a very different lithologic composition (Vorren et al., 1998) than gas hydrate- and gas-bearing contouritic sediment drifts.

This regional best-fit curve is then used to calculate P-wave velocities from S-wave velocities (dotted curve in Figure 11). This curve lies between the ODP reference and the Hamilton curve and provides the background velocities where neither hydrates nor gas is present within the pore space of the sediments. This background trend facilitates a much better reference for estimating gas hydrate and free-gas saturation than can be achieved by using the Hamilton or ODP curve.

The positive difference between P-wave velocity from traveltime inversion and background velocity attributed to the presence of hydrates in the layer above the BSR is 56 m/s, exceeding the estimated uncertainty on the velocity of 25 m/s (gray area in Figure 11). The negative velocity difference underneath the BSR of about 320 m/s is attributed to the presence of gas (Figure 11). The difference for the other layers lies below the average velocity uncertainty. This supports our interpretation that hydrates are confined to the layer just above the BSR, overlying free-gas-containing sediments.

We also calculated the velocity deviation attributed to hydrates and gas at the other OBS stations. The maximum velocity deviations for OBS JM517 equaled 104 m/s for the hydrate-bearing zone and 390 m/s for the gas-bearing zone. OBS JM523 and OBS JM524 showed slightly lower deviations of about 30 m/s for the hydrate-bearing zone and a deviation of up to 400 m/s for the gas-bearing zone.

To conclude, systematic positive and negative velocity deviations occur along the BSR and are interpreted to be caused by the presence of gas hydrate and gas, respectively, within the sediments at the northern flank of the Storegga Slide. The hydrate zone reaches a thickness of up to 50 m, and the gas-charged zone is up to 90 m thick. The presence of both hydrates and gas apparently does not affect the S-wave velocity within sediments of the northern Storegga sidewall.

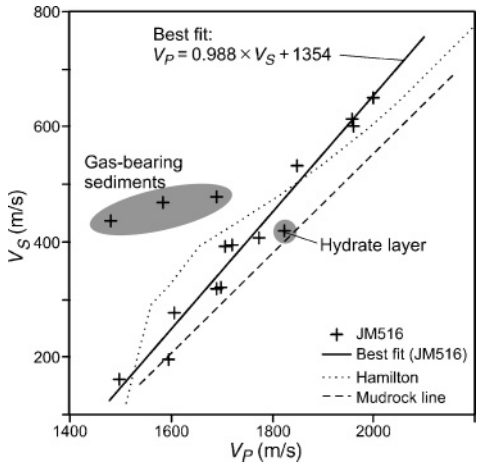

Figure 12. Crossplot of P- and S-wave velocities of OBS JM516 compared to Castagna's mudrock line (1985) and the Hamilton equations (1979). Velocities for gas-bearing sediments can be distinguished clearly, but also the velocity for the layer that has been interpreted to contain gas hydrates lies slightly off the general velocity trend. Velocities of the remaining layers are distributed along this trend within the bounds of the error margins. The least-squares best fit, calculated from velocities not including the gas- and hydrate-bearing sediments, does not correlate with either the mudrock line or the Hamilton curve.

Distribution and concentration of gas hydrates and free gas

Three different rock-physical models have been proposed for hydrated sediments (Ecker et al., 1998; Helgerud et al., 1999; Carcione and Tinivella, 2000; Jakobsen et al., 2000):

1) Hydrates are located in the pore volume without appreciable grain contact and affect the compressibility of the pore fluid.
2) Hydrates act as sediment grains and alter the elastic properties of the mineral phase.
3) Hydrates act as a cement between the sediment grains and strongly increase the stiffness of the matrix.

To convert observed velocity deviations into mean gas hydrate and gas concentrations, we use Tinivella's (1999) weighted-equation approach and Helgerud's effective-medium model (Helgerud et al., 1999; Ecker et al., 2000). Calculated concentrations differ substantially with the rock-physical model applied. Estimates of hydrate concentration decrease from the first model to the third. A strong increase in both seismic velocities even at very low concentrations is expected for the third model (Ecker et al., 1998; Carcione and Tinivella 2000). Our data show an increase in P-wave velocity only and not in S-wave velocity (Figures 10 and 11). This result is supported by the lack of a BSR reflection on the inline component of the OBC data. A sharp interface in shear properties, which is needed to generate shear-wave reflections, is not present. This supports Andreassen et al.'s (2003) findings that hydrates do not cement the sediments, since cementation would result in a distinct increase in S-wave impedance.

Moreover, the S-wave velocity curve seems to be unaffected by the presence of gas hydrates. Even with the second model, the hydrate-as-frame-component model, the S-wave velocity should increase slightly. This S-wave velocity increase is about 1 to 1.5 times the velocity increase of the P-wave. Consequently, the V_P / V_S ratio should decrease in the hydrate layer, but this decrease cannot be observed in the velocity profiles (Figure 11). Hence, our data favor a model in which gas hydrates are disseminated in the pore space of the sediments. This is in contrast with data from the Mallik gas hydrate well, where S-wave velocities clearly increase with gas hydrate saturation (Sakai, 1999). However, gas hydrates at the Mallik site occur within sand layers and in much higher concentrations than at the northern flank of the Storegga Slide, which might suggest a threshold concentration before cementation takes place.

Because of the error margins of the velocity analysis, the preference of the dissemination model cannot be fully assured. Therefore, we provide concentration estimates for both the

hydrate-as-frame-component model and the hydrate-as-pore-fluid-component model. Both estimates offer a range in which the true hydrate concentration can be expected.

The geotechnical borehole (Norwegian Geotechnical Institute, 1997) provides all but two parameters for the modeling (Table 2, Bünz and Mienert, 2004). For the remaining two parameters, we assume the average number of grain contacts is nine and the critical porosity is 40% (Mavko et al., 1998). Density and bulk and shear moduli of the mineral components and hydrates are taken from Mavko et al. (1998), Dvorkin et al. (1999), and Waite et al. (2000). The density and bulk modulus of brine and gas are calculated after Batzle and Wang (1992). Using Helgerud's model (1999), the P-wave velocity calculated for the hydrate-free case is 1762 m/s, which compares remarkably well to the background velocity of 1767 m/s derived from our V_P-V_S relationship. Depending on the end-member model applied, gas hydrate concentrations range between minimum (hydrate-as-frame-component model) and maximum (hydrate-as-pore-fluid-component model) estimates (Table 3). The velocity deviation of 56 m/s at OBS JM516 then yields an average hydrate saturation of pore volume between 6% and 12%. The weighted-equation approach (Tinivella, 1999) gives results very similar to the hydrate-as-frame-component model, with a 5% average hydrate saturation of pore volume. As a result, total bulk hydrate concentration is 3% to 6%. At OBS JM517, hydrate saturation of pore volume is higher, between 11% and 21%, corresponding to 5% to 10% of bulk volume. At OBS JM523 and OBS JM524, the average hydrate saturation ranges between 3% and 8% (1.5% to 4% of bulk volume). A velocity error of 25 m/s in the hydrate layer causes an uncertainty in hydrate concentration of about 2.5% if modeled by the frame model and the weighted-equation approach. The error is up to 5% if hydrate is modeled as the pore-fluid component. The above estimates provide reasonable average hydrate concentrations, but they might still be too high because of an anisotropy effect inherent in wide-angle seismic data in such environments (Holbrook, 2000).

Using Helgerud's model (1999), we can also calculate average gas concentrations. As for hydrate saturations, the concentration of gas depends on which rock-physical model applies. If gas is homogeneously distributed, only very small amounts produce a strong velocity anomaly, whereas if gas occurs in patches, more gas is required to produce the same effect. The modeling parameters for the gas-bearing zone are summarized in Table 2. We observe anomalously low P-wave velocities in two zones beneath the hydrate-bearing sediments (Figures 10 and 11). The first zone is about 30 m thick and shows an average velocity decrease of about 350 m/s, which corresponds to an average concentration of 0.8% of pore space for the homogeneous-gas model and 16% for the patchy-gas model. A velocity decrease of about 220 m/s in the second 40-m-thick zone corresponds to an average concentration of 0.3% for the homogeneous-gas model and 8% for the patchy-gas model. Gas concentrations at individual OBS stations are listed in Table 4. The velocity data do not allow us to distinguish which rock-physical model is appropriate for the sediments at Storegga. Nonetheless, the calculated concentrations can be considered minimum and maximum bounds for the gas saturation in the pore space.

Nature of BSR and enhanced reflections

At the northern flank of the Storegga Slide, the commonly observed reflection patterns at the BGHS show a strong lateral variation in overall appearance, individual reflection amplitude, and waveform (Figures 2, 3, 4, and 13). A distinct BSR as a proper reflection is rarely observed on the high-resolution seismic data (Figure 13a), whereas the vertical component of the lower-resolution OBC shows a clear BSR at the same location on the slope (Figure 13b). This effect is attributable to the different frequency content of the acquisition systems used and has been observed in other gas hydrate areas as well (Vanneste et al., 2001; Chapman et al., 2002; Wood et al., 2002). The dominant wavelengths resolve the structure around the BSR in different ways. The velocity results from inverting the P-wave data and modeling S-wave velocities based on traveltimes and can only give average velocities over layers containing hydrates or gas. Thus, they are useful for estimating the average concentrations of gas hydrates above, and of free gas below, the BSR.

Previous studies of BSRs have shown that the origin of the BSR and the distribution of gas hydrates and free gas can be extracted to some extent from the seismic reflection amplitudes by analyzing the AVO behavior and by modeling the seismic response of a number of probable geologic models for the hydrate/gas interface and the enhanced reflections (Hyndman and Spence, 1992; Singh et al., 1993; Katzman et al., 1994; Minshull et al., 1994; Andreassen et al., 1995; Chapman et al., 2002). The analysis of amplitude behavior can be ambiguous because different models can produce the same AVO behav-

Table 3. Gas hydrate concentrations of pore space at individual OBS stations.

Station	Thickness of hydrate-bearing sediments (m)	Maximum V_P (m/s)	Average velocity effect from hydrates (m/s)	Hydrate concentration* (%)
JM516	47	1823	56	6–12
JM517	56	1884	104	11–21
JM523	42	1815	40	4–8
JM524	32	1791	20	2.5–5

*(Low estimate = hydrate in frame; high estimate = hydrate as pore-fluid component).

Table 4. Gas concentrations of pore space at individual OBS stations.

Station	Thickness of gas-bearing sediments (m)	Minimum V_P (m/s)	Average velocity effect from gas (m/s)	Gas concentration* (%)
JM516	70	1481	320	0.7–14
JM517	90	1415	390	0.9–18
JM523	85	1402	400	0.9–18
JM524	68	1490	310	0.7–14

*(Low estimate = homogeneous distribution; high estimate = patchy distribution).

ior. Reasonable geologic models can be suggested from the seismic observations, and their AVO response can be compared with the real data to circumvent this problem. The two most prominent models proposed for the hydrate/free-gas interface are (1) the hydrate wedge model, in which gas is supposed to be absent underneath the BSR, and (2) a model having a free-gas-containing layer underneath the BSR (Hyndman and Spence, 1992; Singh et al., 1993; Katzman et al., 1994). Recent research suggests a transition zone of about 4 to 8 m with a gradual decrease in velocity (Chapman et al., 2002). Different seismic resolutions can provide a different picture, however, and one needs to consider that the distribution of free gas might be much more complex.

We do not observe a proper BSR on the high-resolution SCS data (Figures 2, 4a, and 13a) but instead a number of so-called enhanced reflections. This fact suggests that gas is not only trapped underneath hydrate-bearing sediments but that it is also trapped within some lithologic units. These units can be traced upward through the BSR (e.g., circle in Figure 13a), and they probably favor the accumulation and migration of gas because of their physical and geological properties, e.g., they might be more permeable than other strata (Bouriak et al., 2000; Bünz and Mienert, 2004). Underneath the BSR, the distance between high-amplitude reflections varies (Figures 2, 4a, and 13a). The reflection amplitude above the BSR is often much lower than underneath, where the presence of gas significantly increases the impedance contrast and we observe much higher amplitudes with reversed polarity. We observe the same effect on the OBS data (Figure 13c; one horizon has been flattened to facilitate the direct comparison of waveforms and amplitudes). On OBS JM517, an enhanced reflection emerges at an offset at about 500 m (Figure 13c). Given the location of the OBS on the upslope line JM99-094, we can identify the proper reflection (circle in Figure 13a). This implies that on this OBS data set, there is no unique reflection from the BGHS separating gas hydrates and gas. As a matter of fact, it is also here that the enhanced reflections terminate.

We have interpreted the significant increase in P-wave velocity observed directly above the BSR to be caused by partial gas hydrate saturation, and the significant decrease in P-wave velocity underneath the BSR to be caused by free gas concentrations (Figure 11). To explain the lack of a proper BSR, we can consider that reflections are caused by gas that is unevenly distributed within specific lithologic units underneath the hydrate-bearing sediments. We anticipate that permeability contrasts between strata control gas distribution and migration (Bouriak et al., 2000; Bünz and Mienert, 2004) such that gas concentration might vary considerably directly underneath the BGHS.

If gas were absent underneath the hydrates, the small amount of hydrate disseminated in the pore space would not allow for the large changes in acoustic impedance. In areas with similar amounts of hydrates, a hydrate-wedge model has been suggested (Korenaga et al., 1997). Even at higher concentrations of hydrates at the BGHS, hydrates account for only 15% of the impedance contrast at the BSR (Holbrook, 2000). Thus, only very high concentrations of hydrates seem to be able to produce perceptible amplitude effects (Hornbach et al., 2003). Both our S-wave velocity data (Figure 11) and the lack of a BSR on the inline component of the OBC data (Figure 3) suggest that gas hydrates do not concentrate in appreciable amounts at the BGHS or at any other level above. Ultimately, hydrates seem to cause only a very minor fraction of observed amplitude anomalies at the BGHS. To conclude, the amplitude anomalies and enhanced reflections are largely caused by underlying free gas.

The strong amplitude reflections on the seismic data are also very likely the result of complex interference within and between the gas-bearing layers, and the OBS and SCS data provide constraints on the thickness of those layers. Two closely spaced enhanced reflections can be discriminated on the OBS data (Figure 13c). Both show a phase reversal compared to the seafloor reflection, indicating a negative impedance contrast at both boundaries. An amplitude increase with offset is clearly recognized for the upper one (Figure 13c). This indicates a two-step decrease in P-wave velocity and suggests an increasing gas concentration with depth.

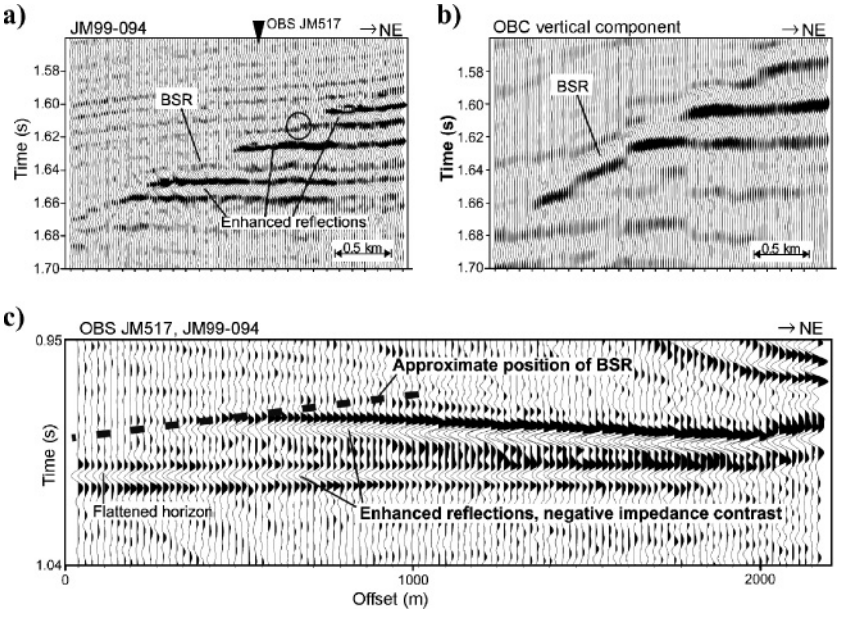

Figure 13. Examples of reflection amplitudes and waveforms from the BGHS. (a,b) The same part of the slope, demonstrating the different appearance of the BSR when imaged with different resolution. Whereas the high-resolution SCS data show the BSR as the termination of enhanced reflections, the OBC line shows a proper BSR reflection. (c) The positive offset of OBS JM517 on the upslope line JM99-094 does not show a clear reflection at the BSR; instead, it mainly consists of high-amplitude reflections that are interpreted to be caused by free gas. The circle in (a) indicates the reflection appearing on the OBS data at an offset of 500 m in (c). The two negative-impedance contrasts indicate a two-step decrease of seismic velocity. The amplitude behavior changes considerably along the line. One horizon has been flattened to facilitate the direct comparison of waveforms and amplitudes.

This contrasts with models in which the gas concentration directly underneath the hydrate is highest or in which a gradual decrease in gas concentration within a small 4- to 8-m zone has been proposed (Korenaga et al., 1997; Chapman et al., 2002). The velocity data (Figure 11) do not show such a two-step decrease because the resolution is too low. The low-velocity layer underneath the BSR has a thickness of 27 m.

Two reflections are resolvable if the thickness of the layer is greater than one-fourth the dominant wavelength. The thickness between layers can be determined by measuring the time interval between the top and the bottom of the layer. The two enhanced reflections of OBS JM517 (Figure 13c) interfere at larger offsets (>2000 m), which is the result of moveout. We find a time lag of 18 ms between them, resulting in a layer thickness of approximately 13 m. This is based on extrapolating the upper reflection to zero offset by following the corresponding lithologic horizon. By neglecting the fact of gradual variations for a moment, this is a good estimate for the maximum thickness of this gas-bearing layer because two distinctly separated enhanced reflections appear nowhere else. The theoretical resolution of our SCS and OBS data should be as low as 4 m but practically is probably a bit lower. The sequence of enhanced reflections on the SCS data that cannot be clearly separated might, therefore, result from gas layers of thicknesses between 2 and 8 m. We can presumably exclude interbed multiples as a sole cause for some enhanced reflections because most of them appear farther downslope underneath the BSR than the overlying ones. On the other side, the tuning effect (Widess, 1973) might certainly contribute to the observed amplitudes. Those 2–13-m thin, gas-bearing layers might internally be much more complex, but this is beyond the resolution of our seismic data. It is also impossible to estimate the exact thickness because we do not know the exact source wavelet and would need a calibration point for the reflectivity.

Analysis of AVO behavior of OBS data

Modeling AVO behavior has two purposes. First, to confirm the velocity profiles by deriving the elastic parameters from the P-wave component alone and comparing them with velocities determined from inversion and modeling; second, to check if a strong negative impedance contrast caused by the presence of gas causes a substantial increase in the absolute reflection amplitude with offset. Accurate isotropic reflection coefficients are calculated from the Zoeppritz equations. However, for explaining the AVO behavior, Bortfeld's approximation (1961) provides more insight, since this relationship writes the reflection coefficient in terms of a fluid and a rigid term:

$$R(\theta) = \underbrace{\frac{1}{2}\ln\left[\frac{\alpha_2\rho_2\cos\theta_1}{\alpha_1\rho_1\cos\theta_2}\right]}_{\text{Fluid factor}} + \underbrace{\left(\frac{\sin\theta_1}{\alpha_1}\right)^2\left(\beta_1^2-\beta_2^2\right)\left(2+\frac{\ln\left(\rho_2/\rho_1\right)}{\ln\left(\beta_2/\beta_1\right)}\right)}_{\text{Rigidity}}, \quad (3)$$

where $R(\theta)$ is the reflection coefficient, α is P-wave velocity, β is S-wave velocity, ρ is density, θ_1 is the incident angle, θ_2 is the reflected or transmitted angle, and the indices α, β, and ρ denote upper (1) and lower (2) half-space.

The fluid factor depends mainly on the P-wave velocity contrasts and hence on the contrasts of the total bulk modulus of

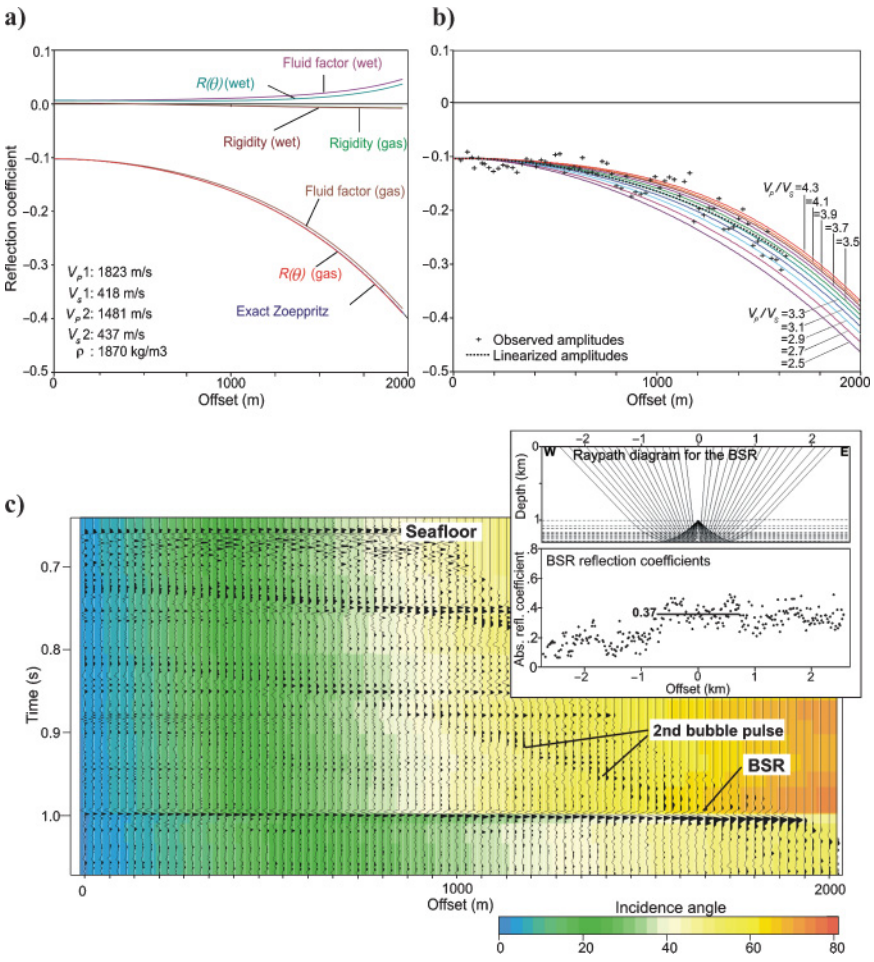

Figure 14. (a) The AVO behavior for the shallow subsurface is dominated by the pore fill of the porous rocks. Note that the rigidity contribution is the same for the gas and the wet case. (b) The AVO behavior of the pressure component indicates the existence of gas but also fits the S-wave velocities determined during forward modeling. The given V_P/V_S ratios change with S-wave velocity in the lower half-space. (c) Muted positive-offset section of the pressure component with NMO corrections applied. The colored background indicates the angle of incidence for the OBS geometry. Raypath diagram shows the spread of reflection points along the BSR. In the area where the BSR is covered by the rays of the OBS experiment, an average BSR reflection coefficient of −0.37 has been determined from the SCS data.

the rock matrix and the pore fluid. The rigidity term shows a strong dependence on S-wave velocities and hence on the shear modulus of the rock matrix. In the shallow subsurface, the pore-fluid contribution to the total bulk modulus is strong. In contrast, the S-wave velocity contrast in unconsolidated sediments is expected to be minimal and the rigidity term is small. Consequently, strong changes in the total bulk modulus through changes of the pore-fluid bulk modulus dominate the AVO response. Such changes occur when gas partly replaces the brine.

In Figure 14a we show the AVO response for the P- and S-wave velocities of OBS JM516. The density is kept fixed at 1870 kg/m^3 (Norwegian Geotechnical Institute, 1997) across the hydrate/gas boundary. For the determined velocities of OBS JM516, the total reflection amplitude is strongly dominated by the fluid factor. The maximum contribution of the rigidity at 2000-m offset is less than 2%. The dominance is even clearer in the case where quasi-hydrates and gas in the pore space have been replaced with brine by using the background P-wave velocity derived from the empirical relation of P-wave and S-wave velocities found earlier. The rigidity curve for this wet case equals that for the gas case.

The shape of the AVO curve for the gas case is similar to the shapes calculated for the hydrate/gas boundary, where the hydrates are disseminated in the pore space (Ecker et al., 1998; Carcione and Tinivella, 2000). However, the P-wave amplitude is extremely sensitive to small amounts of free gas in the pore space; only the vertical incidence reflection coefficient, not the type of anomaly, changes with free-gas saturation. If small amounts of gas are present, AVO behavior is dominated by the gas and only high amounts of gas hydrates (>20% saturation) affect the AVO anomaly. Alternatively, if hydrates cement the sediments, fairly low amounts of hydrates are sufficient to cause a significant increase in both P- and S-wave velocity (Ecker et al., 1998). This would affect the type of anomaly because the rigidity term would increase from a stronger S-wave velocity contrast. A strong S-wave velocity contrast would, in turn, suggest a strong reflection on the inline component of OBC and OBS data, but this is not the case (Figure 3). Thus, the shape of the AVO curve is in agreement with our derived hydrate and gas concentrations and also supports that the BSR originates primarily from the gas. In addition, we can evaluate to some degree whether the observed AVO behavior matches the expected AVO anomaly for the hydrate/gas boundary and how S-wave velocities from forward modeling compare to those derived from the amplitude analysis.

The data at positive offsets on the hydrophone component of OBS JM516 show a high-amplitude reflection at about 1 s. The single reflection event is easily traceable over the section. It corresponds to the high-amplitude reflection on line JM99-095 (Figure 4b) that is associated with the BSR. We assume that on this along-slope line, the high-amplitude reflection on the OBS data corresponds to the BSR. Furthermore, since it is a single event and the waveform does not change, it seems not to be affected by tuning as observed on the other OBS data (Figure 13c). BSR amplitudes were picked on OBS JM516 where they are not distorted by the bubble pulse. This corresponds to angles of incidence up to 60° or offsets of nearly 1600 m, which are sufficient for analyzing AVO behavior (Figure 14b).

Reflection coefficients of the BSR were determined by the method of Warner (1990) (Figure 14b). The reflection point of the AVO data is spread out between 0 and 0.5 km. No large reflectivity variation occurs within this range; thus, no respective corrections are applied to the AVO data. Finally, because we cannot assess the exact normal-incidence reflection coefficient, the AVO data are scaled linearly for direct comparison with our model. Bearing in mind the problems of deriving the AVO behavior from geometric considerations and amplitude effects at the gas hydrate/free-gas boundary, we find the shape of the AVO anomaly of the OBS data approximates the modeled AVO curve and indicates the existence of free gas (Figure 14c). A linearized fit is derived from the AVO data (Kelly and Skidmore 2001) and compared to a set of models, where V_P/V_S is changed with S-wave velocity in the lower half-space. The best fit is achieved for a V_P/V_S ratio of 3.3, which is in excellent agreement with the V_P/V_S ratio of 3.4 determined by the velocity analysis.

CONCLUSIONS

Inversion, modeling, and amplitude analysis of multicomponent, wide-angle seismic data provide new insights into the vertical distribution and concentration of gas hydrates and free gas at the northern flank of the Storegga Slide area on the mid-Norwegian margin. The combined analysis of P- and S-wave velocities allows us to constrain background velocities for hydrate-free and gas-free sediments and thus make hydrate and gas quantifications more reliable. The velocities obtained also improve the distinction between three rock-physical models for hydrate-bearing sediments: (1) hydrates are part of the pore fluid, (2) hydrates are part of the sediment frame without considerably affecting the shear strength, or (3) hydrates cement between sediment grains.

Our results indicate that gas hydrates likely occur at the northern flank of the Storegga Slide and that they are concentrated in an approximately 50-m-thick zone directly above the BSR, having partial hydrate concentrations of about 3% to 6% of pore space when modeled by weighted-equation theory or effective-medium theory, assuming hydrates as a component of the sediment frame. Concentrations are 6% to 12% when modeled, assuming hydrates as a component of the pore fluid. Hydrates are most likely disseminated, neither cementing the sediment matrix nor affecting the stiffness of the matrix noticeably.

Average free-gas concentrations beneath the hydrate stability zone are about 0.4% to 0.8% of pore volume assuming homogeneous gas distribution or are up to 18% of pore volume if the gas is assumed to be patchily distributed. The average thickness of the free-gas zone underneath the BSR is approximately 80 m. Amplitude and reflectivity analyses suggest a rather complex distribution of gas. While higher gas concentrations are generally expected directly beneath the hydrate-bearing sediments, our data reveal that the gas concentration increases slightly with depth at certain locations. In some places, the thickness of the gas-bearing layers underneath the BSR can be distinguished clearly, but in others it might be as thin as about 2 m. Gas is distributed predominantly along strata and not along the BGHS underneath the hydrates. The gas in the strata significantly increases the impedance contrast, causing enhanced reflections on the seismic reflection

data. The reflection enhancement terminates at the level of the BGHS, where hydrates overlie and possibly trap gas, causing the BSR to be observed as an envelope of those terminations rather than a distinct reflection. Our data also illustrate that the origin of the BSR is largely the result of the trapped gas underneath.

ACKNOWLEDGMENTS

We gratefully acknowledge the professional and enthusiastic support of the ship captains and crew of the R/V *Jan Mayen* during our fieldwork. Insightful reviews by Graham Westbrook, Ralph Stephen, and Jose Carcione helped to improve an earlier version of the manuscript. We also thank Yonghe Sun, Christian Berndt, Ingo Pecher, William Dillon, and an unknown reviewer for their valuable and helpful reviews. The University of Tromsø acknowledges support by Landmark Graphics via the Landmark University Grant Program. We are grateful to Petroleum Geo-Services (PGS) for providing the ocean-bottom cable data and software. Norsk Hydro is acknowledged for providing both seismic reflection data and geotechnical information. The GMT software (Wessel and Smith, 1991) was used to create maps in Figure 1. S. B. benefitted from a 5-month visit at Woods Hole Oceanographic Institution. The work was funded by Norwegian Research Council grant 128164/432, European Community grant EVK3-CT-1999-00006 (COSTA project), and Norsk Hydro grant NHT-B44-VK0768-00.

REFERENCES

Aki, K., and P. G. Richards, 2002, Quantitative seismology: University Science Books.

Andreassen, K., K. A. Berteussen, H. Sognnes, K. Henneberg, J. Langhammer, and J. Mienert, 2003, Multi-component ocean bottom cable data in gas-hydrate investigation: Journal of Geophysical Research, **108**, 2399, doi:10.1029/2002JB002245.

Andreassen, K., P. E. Hart, and A. Grantz, 1995, Seismic studies of a bottom simulating reflection related to gas hydrate beneath the continental margin of the Beaufort Sea: Journal of Geophysical Research, **100**, 12659–12673.

Andreassen, K., J. Mienert, P. Bryn, and S. C. Singh, 2000, A double gas-hydrate related bottom simulating reflector at the Norwegian continental margin: Annals of the New York Academy of Science, **912**, 126–135.

Anstey, N. A., 1991, Velocity in a thin section: First Break, **9**, 449–457.

Batzle, M., and Z. J. Wang, 1992, Seismic properties of pore fluids: Geophysics, **57**, 1396–1408.

Berndt, C., S. Bünz, and J. Mienert, 2003, Polygonal fault systems on the mid-Norwegian margin: A long-term source for fluid flow, *in* P. Van Rensbergen, R. Hillis, A. Maltman, and C. Morley, eds., Subsurface sediment mobilization: Geological Society of London Special Publication 216, 283–290.

Berndt, C., J. Mienert, M. Vanneste, S. Bünz, and P. Bryn, 2002, Submarine slope failure offshore Norway triggers rapid gas hydrate decomposition: Fourth International Conference on Gas Hydrates, Proceedings, 71–74.

Blystad, P., H. Brekke, R. B. Færseth, B. T. Larsen, J. Skogseid, and B. Tørudbakken, 1995, Structural elements of the Norwegian continental shelf, II: The Norwegian Sea region: Norwegian Petroleum Directorate Bulletin 8.

Bondevik, S., J. I. Svendsen, G. Johnsen, J. Mangerud, and P. E. Kaland, 1997, The Storegga tsunami along the Norwegian coast: Its age and runup: Boreas, **26**, 29–53.

Bortfeld, R., 1961, Approximations to the reflection and transmission coefficients of plane longitudinal and transverse waves: Geophysical Prospecting, **9**, 485–503.

Bouriak, S., M. Vanneste, and A. Saoutkine, 2000, Inferred gas hydrates and clay diapirs near the Storegga Slide on the southern edge of the Vøring plateau, offshore Norway: Marine Geology, **163**, 125–148.

Brekke, H., 2000, The tectonic evolution of the Norwegian Sea continental margin with emphasis on the Vøring and Møre basins, *in* A. Nøttvedt, ed., Dynamics of the Norwegian margin: Geological Society of London Special Publication 167, 327–378.

Brekke, H., and F. Riis, 1987, Tectonics and basin evolution of the Norwegian shelf between 62 degrees N and 72 degrees N: Norsk Geologisk Tidskrift, **67**, 295–321.

Bryn, P., S. R. Østmo, R. Lien, K. Berg, and T. I. Tjelto, 1998, Slope stability in the deep water areas off mid-Norway: Offshore Technology Conference, Proceedings, paper 8640.

Bryn, P., A. Solheim, K. Berg, R. Lien, C. F. Forsberg, H. Haflidason, D. Ottesen, and L. Rise, 2003, The Storegga Slide complex: Repeated large scale sliding in response to climatic cyclicity, *in* J. Locat and J. Mienert, eds., Submarine mass movements and their consequences: Kluwer Academic Publishers, 215–222.

Bugge, T., R. H. Belderson, and N. H. Kenyon, 1988, The Storegga Slide: Philosophical Transactions of the Royal Society of London Series A, **325**, 357–388.

Bünz, S., and J. Mienert, 2004, Acoustic imaging of gas hydrates and free gas at the Storegga Slide: Journal of Geophysical Research, **109**, B04102, doi:10.1029/2003JB002863.

Bünz, S., J. Mienert, and C. Berndt, 2003, Geological controls on the Storegga gas-hydrate system of the mid-Norwegian continental margin: Earth and Planetary Science Letters, **209**, 291–307.

Carcione, J. M., and U. Tinivella, 2000, Bottom-simulating reflectors: Seismic velocities and AVO effects: Geophysics, **65**, 54–67.

Castagna, J. P., M. L. Batzle, and R. L. Eastwood, 1985, Relationships between compressional-wave and shear-wave velocities in clastic silicate rocks: Geophysics, **50**, 571–581.

Chapman, N. R., J. F. Gettrust, R. Walia, D. Hannay, G. D. Spence, W. T. Wood, and R. D. Hyndman, 2002, High-resolution, deep-towed, multichannel seismic survey of deep-sea gas hydrates off western Canada: Geophysics, **67**, 1038–1047.

Dalland, A., D. Worsley, and K. Ofstad, 1988, A lithostratigraphic scheme for the Mesozoic and Cenozoic succession offshore mid- and northern Norway: Norwegian Petroleum Directorate Bulletin 4.

Doré, A. G., and E. R. Lundin, 1996, Cenozoic compressional structures on the NE Atlantic margin: Nature, origin and potential significance for hydrocarbon exploration: Petroleum Geoscience, **2**, 299–311.

Dvorkin, J., M. Prasad, A. Sakai, and D. Lavoie, 1999, Elasticity of marine sediments: Rock physics modeling: Geophysical Research Letters, **26**, 1781–1784.

Ecker, C., J. Dvorkin, and A. Nur, 1998, Sediments with gas hydrates: Internal structure from seismic AVO: Geophysics, **63**, 1659–1669.

———, 2000, Estimating the amount of gas hydrate and free gas from marine seismic data: Geophysics, **65**, 565–573.

Eldholm, O., J. Thiede, and E. Taylor, 1987, The Norwegian Sea: Proceedings of the Ocean Drilling Project, Initial Results 104.

Engelmark, F., 2001, Using 4-C to characterize lithologies and fluids in clastic reservoirs: The Leading Edge, **20**, 1053–1055.

Evans, D., S. McGiveron, Z. Harrison, P. Bryn, and K. Bjerg, 2002, Along-slope variation in the late Neogene evolution of the mid-Norwegian margin in response to uplift and tectonism, *in* A. G. Doré, J. A. Cartwright, M. S. Stoker, J. P. Turner, and N. J. White, eds., Exhumation of the North Atlantic Margin: Timing, mechanisms and implications for petroleum exploration: Geological Society of London Special Publication 196, 139–151.

Flüh, E. R., D. Klaeschen, and J. Bialas, 2002, Options for multicomponent seismic data acquisition in deep water: First Break, **20**, 764–769.

Gaiser, J. E., 1999, Applications for vector coordinate systems of 3-D converted-wave data: The Leading Edge, **18**, 1290–1300.

Gaiser, J., N. Moldoveanu, C. Macbeth, R. Michelena, and S. Spitz, 2001, Multicomponent technology: The players, problems, applications, and trends: The Leading Edge, **20**, 974.

Haflidason, H., H. P. Sejrup, A. Nygard, J. Mienert, P. Bryn, R. Lien, C. F. Forsberg, K. Berg, and D. Masson, 2004, The Storegga Slide: Architecture, geometry and slide development: Marine Geology, **213**, 201–234.

Hamilton, E. L., 1976, Shear-wave velocity versus depth in marine sediments: A review: Geophysics, **41**, 985–996.

———, 1979, V_P/V_S and Poisson's ratios in marine sediments and rocks: Journal of the Acoustic Society of America, **66**, 1093–1100.

Han, D., A. Nur, and D. Morgan, 1986, Effects of porosity and clay content on wave velocities in sandstones: Geophysics, **51**, 2093–2107.

Helgerud, M. B., J. Dvorkin, A. Nur, A. Sakai, and T. Collett, 1999, Elastic-wave velocity in marine sediments with gas hydrates: Effective medium modeling: Geophysical Research Letters, **26**, 2021–2024.

Hjelstuen, B. O., O. Eldholm, and J. Skogseid, 1999, Cenozoic evolution of the northern Vøring margin: Geological Society of America Bulletin, **111**, 1792–1807.
Holbrook, W. S., 2000, Seismic studies of the Blake Ridge: Implications for hydrate distribution, methane expulsion, and free gas dynamics, *in* C. K. Paull and W. P. Dillon, eds., Natural gas hydrates: Occurrence, distribution, and detection: American Geophysical Union, Geophysics Monograph 124, 235–256.
Holbrook, W. S., H. Hoskins, W. T. Wood, R. A. Stephen, and D. Lizarralde, 1996, Methane hydrate and free gas on the Blake ridge from vertical seismic profiling: Science, **273**, 1840–1843.
Hornbach, M. J., W. S. Holbrook, A. R. Gorman, K. L. Hackwith, D. Lizarralde, and I. Pecher, 2003, Direct seismic detection of methane hydrate on the Blake ridge: Geophysics, **68**, 92–100.
Hyndman, R. D., and G. D. Spence, 1992, A seismic study of methane hydrate marine bottom simulating reflectors: Journal of Geophysical Research, **97**, 6683–6698.
Jakobsen, M., J. A. Hudson, T. A. Minshull, and S. C. Singh, 2000, Elastic properties of hydrate-bearing sediments using effective medium theory: Journal of Geophysical Research, **105**, 561–577.
Katzman, R., W. S. Holbrook, and C. K. Paull, 1994, Combined vertical-incidence and wide-angle seismic study of a gas hydrate zone, Blake ridge: Journal of Geophysical Research, **99**, 17975–17995.
Kelly, M. C., and C. Skidmore, 2001, Non-linear AVO equations and their use in three-parameter inversions: 71st Annual International Meeting, SEG, Expanded Abstracts, 255–256.
Kennett, J. P., K. G. Cannariato, I. L. Hendy, and R. J. Behl, 2003, Methane hydrates in Quaternary climate change: The Clathrate gun hypothesis: American Geophysical Union Special Publication 54.
Korenaga, J., W. S. Holbrook, S. C. Singh, and T. A. Minshull, 1997, Natural gas hydrates on the southeast US margin: Constraints from full waveform and traveltime inversions of wide-angle seismic data: Journal of Geophysical Research, **102**, 15345–15365.
Kvenvolden, K. A., 1993, Gas hydrates — Geological perspective and global change: Review of Geophysics, **31**, 173–187.
Laberg, J. S., T. Dahlgren, T. O. Vorren, H. Haflidason, and P. Bryn, 2001, Seismic analyses of Cenozoic contourite drift development in the northern Norwegian Sea: Marine Geophysical Research, **22**, 401–416.
MacLeod, M. K., R. A. Hanson, C. R. Bell, and S. Mchugo, 1999, The Alba field ocean bottom cable seismic survey: Impact on development: The Leading Edge, **18**, 1306–1312.
Mavko, G., T. Mukerji, and J. Dvorkin, 1998, The rock physics handbook: Cambridge University Press.
Mienert, J., and P. Bryn, 1997, Gas hydrate drilling conducted on the European margin: EOS Transactions of the American Geophysical Union, **78**, 567.
Mienert, J., J. Posewang, and M. Baumann, 1998, Gas hydrates along the northeastern Atlantic Margin: Possible hydrate-bound margin instabilities and possible release of methane, *in* J. P. Henriet, and J. Mienert, eds., Gas hydrates: Relevance to world margin stability and climate change: Geological Society of London Special Publication 137, 275–291.
Mienert, J., J. Posewang, and D. Lukas, 2001, Changes in the hydrate stability zone on the Norwegian Margin and their consequences for methane and carbon releases into the oceanosphere, *in* P. Schäfer, W. Ritzrau, M. Schlüter, and J. Thiede, eds., The northern north Atlantic: A changing environment: Springer Press, 259–280.
Minshull, T. A., S. C. Singh, and G. K. Westbrook, 1994, Seismic velocity structure at a gas hydrate reflector, offshore western Colombia, from full-wave-form inversion: Journal of Geophysical Research, **99**, 4715–4734.
Müller, C., F. Theilen, and B. Milkereit, 2001, Combined vertical-incidence and wide-angle seismic study of deepwater bright-spot reflections: The Leading Edge, **20**, 854–857.
Norwegian Geotechnical Institute, 1997, Møre and Vøring soil investigation: Report 972521–1.
Posewang, J., and J. Mienert, 1999, The enigma of double BSRs: Indicators for changes in the hydrate stability field?: Geo-Marine Letters, **19**, 157–163.
Rokoengen, K., L. Rise, P. Bryn, B. Frengstad, B. Gustavsen, E. Nygaard, and J. Saettem, 1995, Upper Cenozoic stratigraphy on the mid-Norwegian continental shelf: Norsk Geologisk Tidskrift, **75**, 88–104.
Sakai, A., 1999, Velocity analysis of vertical seismic profile (VSP) survey at JAPEX/JNOC/GSC Mallik 2L-38 gas hydrate research well, and related problems for estimating gas hydrate concentration: Geological Survey of Canada Bulletin, **544**, 323–340.
Singh, S. C., T. A. Minshull, and G. D. Spence, 1993, Velocity structure of a gas hydrate reflector: Science, **260**, 204–207.
Skogseid, J., and O. Eldholm, 1989, Vøring Plateau continental margin: Seismic interpretation, stratigraphy, and vertical movements, *in* O. Eldholm, J. Thiede, and E. Taylor, eds., The Norwegian margin: Proceedings of the ODP, Scientific Results, **104**, 993–1030.
Sloan, E. D., 1998, Gas hydrates: Review of physical/chemical properties: Energy & Fuels, **12**, 191–196.
Stewart, R. R., J. E. Gaiser, R. J. Brown, and D. C. Lawton, 2002, Converted-wave seismic exploration: Methods: Geophysics, **67**, 1348–1363.
———, 2003, Converted-wave seismic exploration: Applications: Geophysics, **68**, 40–57.
Stuevold, L. M., and O. Eldholm, 1996, Cenozoic uplift of Fennoscandia inferred from a study of the mid-Norwegian margin: Global and Planetary Change, **12**, 359–386.
Tatham, R. H., 1982, V_P/V_S and lithology: Geophysics, **47**, 336–344.
Tatham, R. H., and P. L. Stoffa, 1976, V_P-V_S — Potential hydrocarbon indicator: Geophysics, **41**, 837–849.
Thomsen, L., 1999, Converted-wave reflection seismology over inhomogeneous, anisotropic media: Geophysics, **64**, 678–690.
Tinivella, U., 1999, A method for estimating gas hydrate and free gas concentrations in marine sediments: Bolletino di Geofisica Teoretica ed Applicata, **40**, 19–30.
Tréhu, A. M., G. Bohrmann, and shipboard scientific party, 2002, Drilling gas hydrates on hydrate ridge, Cascadia continental margin: Ocean Drilling Project Preliminary Report 204.
Vågnes, E., R. H. Gabrielsen, and P. Haremo, 1998, Late Cretaceous–Cenozoic intraplate contractional deformation at the Norwegian continental shelf: Timing, magnitude and regional implications: Tectonophysics, **12**, 29–46.
Vanneste, M., M. De Batist, A. Golmshtok, A. Kremlev, and W. Versteeg, 2001, Multi-frequency seismic study of gas hydrate-bearing sediments in Lake Baikal, Siberia: Marine Geology, **172**, 1–21.
Vogt, P. R., and W. Y. Jung, 2002, Holocene mass wasting on upper non-polar continental slopes — Due to post-glacial ocean warming and hydrate dissociation? Geophysical Research Letters, **29**, doi:10.1029/2001GL013488.
Vorren, T. O., J. S. Laberg, F. Blaume, J. A. Dowdeswell, N. H. Kenyon, J. Mienert, J. Rumohr, and F. Werner, 1998, The Norwegian Greenland Sea continental margins: Morphology and late Quaternary sedimentary processes and environment: Quaternary Science Reviews, **17**, 273–302.
Waite, W. F., M. B. Helgerud, A. Nur, J. C. Pinkston, L. A. Stern, S. H. Kirby, and W. B. Durham, 2000, Laboratory measurements of compressional and shear wave speeds through methane hydrate: Annals of the New York Academy of Science, **912**, 1003–1010.
Ward, S. N., 2001, Landslide tsunami: Journal of Geophysical Research, **106**, 11201–11215.
Warner, M., 1990, Absolute reflection coefficients from deep seismic reflections: Tectonophysics, **173**, 15–23.
Wessel, P., and W. H. F. Smith, 1991, Free software helps map and display data: American Geophysical Union, EOS Transactions, **72**, 441.
Widess, M. B., 1973, How thin is a thin bed: Geophysics, **38**, 1176–1180.
Wood, W. T., J. F. Gettrust, N. R. Chapman, G. D. Spence, and R. D. Hyndman, 2002, Decreased stability of methane hydrates in marine sediments owing to phase-boundary roughness: Nature, **420**, 656–660.
Zelt, C. A., and D. A. Forsyth, 1994, Modeling wide-angle seismic data for crustal structure — Southeastern Grenville province: Journal of Geophysical Research, **99**, 11687–11704.
Zelt, C. A., and R. B. Smith, 1992, Seismic traveltime inversion for 2-D crustal velocity structure: Geophysical Journal International, **108**, 16–34.